Inhomogeneity and Segregation Effect in the Surface Layer of Fe-Doped SrTiO$_3$ Single Crystals

Marcin Wojtyniak [1,2,]*, Katarzyna Balin [1,2], Jacek Szade [1,2] and Krzysztof Szot [1,2]

[1] Institute of Physics, University of Silesia, 75 Pulku Piechoty 1, 41–500 Chorzow, Poland; katarzyna.balin@us.edu.pl (K.B.); jacek.szade@us.edu.pl (J.S.); krzysztof.szot@us.edu.pl (K.S.)

[2] Silesian Center for Education and Interdisciplinary Research, 75 Pulku Piechoty 1a, 41-500 Chorzow, Poland

[*] Correspondence: marcin.wojtyniak@us.edu.pl

Abstract: The effect of Fe doping on SrTiO$_3$ single crystals was investigated in terms of crystal and electronic structure over a wide temperature range in both oxidizing and reducing conditions. The electrical properties were thoroughly studied with a special focus on the resistive switching phenomenon. Contrary to the undoped SrTiO$_3$ crystals, where isolated filaments are responsible for resistive switching, the iron-doped crystals showed stripe-like conducting regions at the nanoscale. The results showed a non-uniform Fe distribution of as-received crystals and the formation of new phases in the surface layer of reduced/oxidized samples. The oxidation procedure led to a separation of Ti(Fe) and Sr, while the reduction resulted in the tendency of Fe to agglomerate and migrate away from the surface as seen from the time of flight mass spectroscopy measurements. Moreover, a clear presence of Fe-rich nano-filament in the reduced sample was found.

Keywords: electronic oxides; strontium titanate; extended defects

1. Introduction

The resistive switching (RS) phenomenon attracts growing interest, and is approaching the level of applied device implementation [1–4]. Attention towards the RS phenomena results from physical mechanisms that can be generally explained as a non-volatile change of the material resistivity under electrical stimuli. A wide variety of materials exhibit such behavior, thus efforts to reveal the nature of this mechanism and explore specific applications is widespread. Nevertheless since the change of resistance in such materials is non-volatile and reversible, they are treated as prospective candidates for the development of non-volatile memory devices, next-generation logic devices and neuromorphic systems [2–5]. Among various materials remarkable advancements have been observed in the field of transition metal oxides [6–8]. SrTiO$_3$ (STO) [9], between other ternary (or binary like TiO$_2$ [10]) transition metal oxides, may be especially suited for memory applications [11]. In addition, the STO is also considered a model material [12] due to its relatively simple structure and a multitude of experimental data [13]. In addition, the effects of various doping such as Nb, La, Cr or Fe are being actively investigated [14–17]. However, no complex report of the influence of the external stimuli (thermal treatment under oxidizing and reducing conditions) on doped STO was made. We believe that only the complex studies will allow shedding of some light onto the basics of the RS phenomena in macro- and nano-scales, and will allow disclosure of how it is related to previous work on the undoped STO [5,18,19]. We have decided to focus on the Fe-doped STO crystals since the Fe oxidation states are relatively easy to determine by many techniques or even by optical examination (crystals with 4+ Fe are very dark, crystals with Fe at lower oxidation states such as 3+ and 2+ are yellow) [20]. Thus, we have investigated STO single crystals with two nominal concentrations of iron (0.13 and 0.45 at%). Naturally, for the application purposes, thin films of STO (especially doped) would be more

beneficial [21], however, single crystals offer the greatest advantage for the interpretation of the origin of such a complicated phenomenon as RS, especially with respect to the insulator-to-metal transition. What is more, STO epitaxial growth requires La- or Nb-doped STO substrates acting as a bottom electrode, which complicates the system as the substrates can also exhibit complex phenomena, such as RS behavior [15,22].

In this work, we have implemented a number of interdisciplinary techniques for determination of the physicochemistry of the surface layer and electrical behavior at the nanoscale. We have focused on the phase and chemistry of investigated crystals by X-ray Diffraction (XRD), X-ray Fluorescence Spectroscopy (XRF) and Time of Flight Secondary Ion Mass Spectroscopy (TOF-SIMS). In addition, we have investigated the electronic structure and electric transport properties by X-ray Photoelectron Spectroscopy (XPS) and Local Conductivity Atomic Force Microscopy (LC-AFM).

2. Materials and Methods

The single crystals of Verneuil grown STO with several nominal concentrations of iron and defined orientation were obtained from various manufacturers (primarily from CrysTec). We focused mainly on the samples doped with 0.13 and 0.45 at% of iron. The investigated samples were annealed in the range of 30 °C to 1100 °C under reducing and oxidizing conditions according to the description in the experiments. It is worth mentioning that the thermal history had significant influence on the crystal properties, thus if not stated otherwise, the thermal treatment was done on fresh batch of crystals for each experiment. For the as-received samples no special treatment was implemented.

The crystal structure was investigated using XRD Empyrean provided by Panalytical in a standard $\theta - 2\theta$ geometry. Cell parameters were determined by the Rietveld method. The electronic structure was investigated by XPS using two spectrometers: PHI 5600 and 5700 provided by Physical Electronics. Both spectrometer implemented monochromatized Al Kα radiation. The chemistry of the surface layer was investigated by the TOF-SIMS using a SIMS-5 spectrometer provided by ION-TOF. Bi$^+$ ion beam was used for the analysis, while Cs$^+$ was applied for depth profiling. The elemental composition of the samples was obtained by the XRF ZSX Primus II provided by Rigaku using the fundamental parameter method. For the surface topography and local conductivity two types of AFM were used, namely JSPM-5200 provided by JEOL and VT AFM XA 50/500 provided by Omicron, both equipped with tips from different manufacturers (Nanosensors, Budget Sensors). In the case of LC-AFM mode, a voltage up to 10 V was applied, although such high voltages are known to modify the surface layer of the material, thus was rarely used. The voltage was typically applied to the conducting AFM tip, whereas the sample holder acted as the second electrode. Finally, the macroscopic electrical measurements were performed by the standard two-point method on a home-built system.

3. Results and Discussion

3.1. As Received Samples

The as-received samples investigated by the XRD in standard geometry showed simple cubic $Pm\bar{3}m$ phase, with a lattice parameter of 0.3904(5) Å at room temperature, which is characteristic for STO structure. No additional component beside the STO structure was found. This result is very similar to undoped STO cell length [23] and no dependency on Fe concentration was found. The impurity analysis showed traces of Ni and Cu (several dozens of ppm). Nevertheless, simple optical investigation shows different sample coloration depending on the Fe content: samples with 0.13 at% Fe were yellow while the 0.45 at% Fe samples exhibited a dark brown color. Closer optical examination revealed also slight color changes which may suggest non-uniform dopant distribution. It is also possible that the different valence state of iron ions affects the crystal color, as it was shown that the darker color corresponds to higher oxidation state [24,25]. Moreover, the color of the crystals strongly depends on its thermal or electrical history, for example in a form of electro-coloration, which is discussed in a separate paper [26]. A most prominent example of the inhomogeneous sample color can be found in Figure 1a for the 0.13

at% Fe doped STO crystal. The same region was measured by the XRF technique in the mapping mode and the results are shown in Figure 1b. We have found a large variation of Fe content, from nominal 0.13–0.8 at%, at relatively short distances (tens of microns), which correlates with the optical image. In addition, the XPS analysis was carried out on all samples. We focused on the Fe *2p* line, however very small concentration of Fe gave poor results. Therefore, the XPS analysis was performed on the sample with the higher Fe content of 0.45% at. The results show Fe/Ti ratio to be close to 0.3 at% (after initial short 300 °C annealing under ultra-high vacuum conditions, UHV) and ratio of 0.4 at% which is very close to the nominal value (after UHV cleaving). Further analysis of the Fe *2p* level photoemission line is presented in Figure 2.
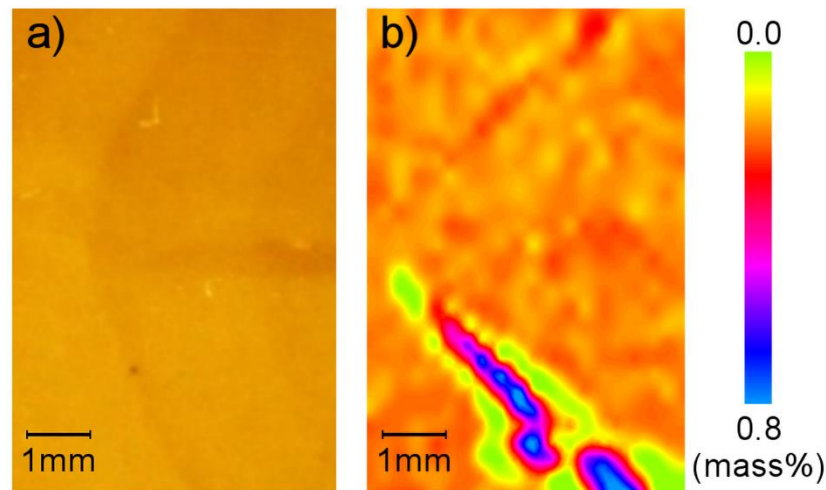

Figure 1. Images of the SrTiO$_3$ single crystal doped with 0.13 at% Fe with the visible inhomogeneity as measured by: (**a**) the optical microscopy and (**b**) XRF technique in the mapping mode showing the Fe concentration map.
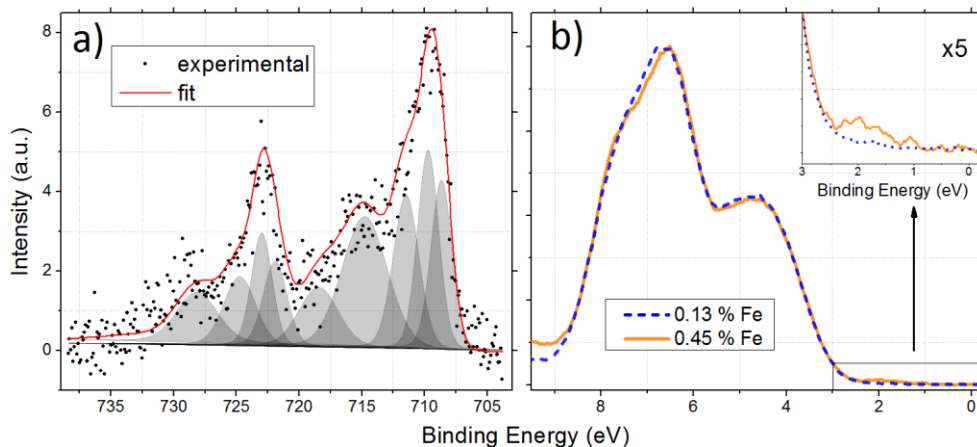

Figure 2. XPS result of SrTiO$_3$ (STO) crystal doped with 0.45 % Fe after short heating (**a**) Fe 2p multiplet together with the results of fitting and; (**b**) the valence band photoemission spectra compared to the lower doping level of 0.13 at% Fe.

The literature shows lack of consensus for the valence state of Fe in STO. The ESR and Mössbauer studies showed oxidation from 2+ up to 5+ [27,28], while the EXAFS studies revealed the 3+ and 4+ Fe ion valency [25]. Thin films of Fe-doped STO measured by XAS and XPS showed the presence of both 2+ and 3+ ions [29,30]. This variation is most probably connected to the presence of the oxygen vacancies, which affect the Fe valence state. A further complication stems from the fact that the iron oxidation state can be relatively easily changed (from 2+ to 4+) by the heat treatment at different atmospheres, as was shown on Sr(Ti,Fe)O$_x$ solid-solution [31]. Thus a thermal history of the sample will

influence the results greatly. Detailed analysis of the Fe *2p* multiplet (for the 0.45 at% Fe crystal) showed a mixture of trivalent and divalent iron ions. The tetravalent state for a Fe ion centering the octahedron was absent, which is evident by comparing our results to the nominal Fe 4^+ that can be found in the $SrFeO_3$ [32,33]. In addition, Figure 2b shows valence band and close-up for the in-gap states vs. the Fe concentration of two crystals. The results show relatively low intensity at the energy gap for both samples and a small dependence on the Fe concentration in the 1–2.5 eV region (inset of Figure 2b). The Ti *2p* and Sr *3d* lines were very similar to the undoped STO crystal, with no sign of reduction of the Ti states. The surface topography measured by the AFM (not shown) showed an atomically flat surface with 3.9 Å height steps, consistent with the cubic unit cell of undoped STO [34].

We also measure the electrical properties of the samples both macroscopically and in nanoscale. Figure 3a shows a typical pseudo-3D current map for the 0.13 at% Fe-doped sample obtained by LC-AFM technique [35]. The brighter spots correlate to nanometer-sized regions with low resistance. It was previously shown in [4] that those regions are related to extended defects, which can act as easy diffusion paths for the oxygen vacancies. The vacancies contribute to the electronic conductivity resulting in large charge transfers (large current). On the other hand, the macroscopic investigation of the as-received samples shows semiconducting behavior shown in Figure 3b as an Arrhenius plot. The resulting activation energy of 0.91 eV is close to the 1.0 eV reported in the literature for STO crystal without doping [4].
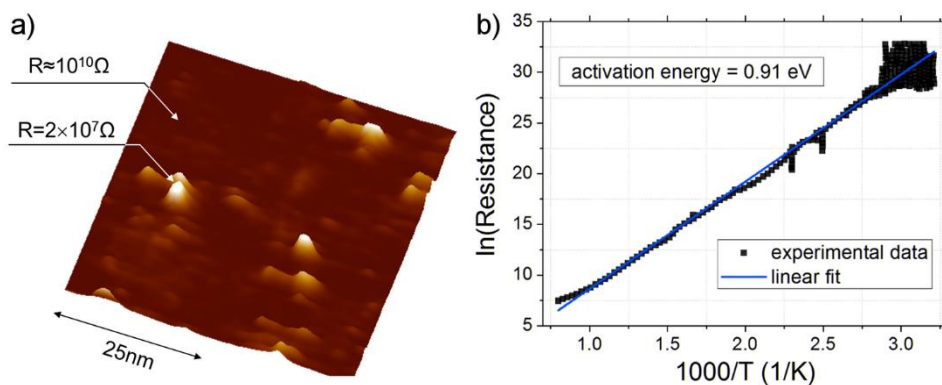

Figure 3. Results from the (**a**) LC-AFM current map at elevated temperature (250 °C) under vacuum (10^{-5} mbar) and (**b**) the Arrhenius plot calculated from the macroscopic resistance measurements of untreated STO doped with 0.13 at% Fe under slightly reduced oxygen partial pressure (p_{O2} = 100 mbar).

3.2. Annealing under Reducing Conditions

The annealing under reducing conditions was achieved under UHV at several temperatures: 125, 250, 500, 750 and 1000 °C. After each heating step was achieved, the sample was cooled to room temperature and measured by the AFM. The evolution of the crystal surface is presented in Figure 4 for the 0.13 at% Fe-doped sample. For low annealing temperatures, similarly to the as-received sample, the surface is atomically flat with steps equal to the STO cell length. The annealing is not affecting the morphology in a significant way up to around 750 °C. Nevertheless, signs of undergoing transformation and the removal of the physi- and chemi-sorbates is visible as a change in the atomic terrace lines. One can notice that the terraces becomes furrowed with increasing annealing temperature. From the effusion experiments (not shown) we know, that at lower temperature mostly water is removed, while above 500 °C mostly carbohydrates are removed. At temperatures above 750 °C the steps become very smooth preserving the step height of 3.9 Å. Those relatively small topographic changes are accompanied by an interesting change in the electrical behavior. The samples annealed at 1000 °C change their character from insulating to conducting as shown in Figure 5a. One can observe emergence of conducting patterns along (100) crystallographic direction with approximately 40 nm distance between the conducting lines. It is worth mentioning that this pattern does not correlate with the surface morphology (surface terraces in particular).
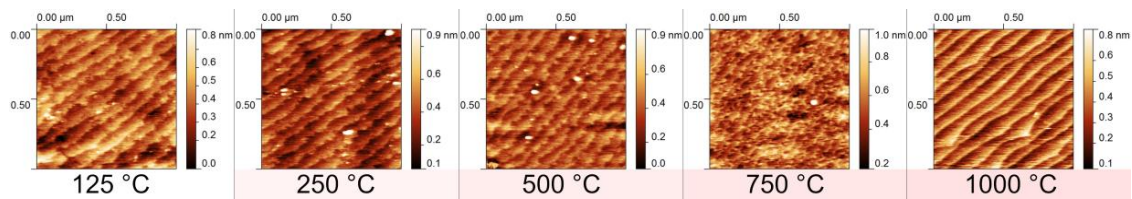
Figure 4. Evolution of surface topography measured for the 0.13 at% Fe-doped STO after thermal treatment ranging from 125 to 1000 °C under UHV conditions (10^{-10} mbar).
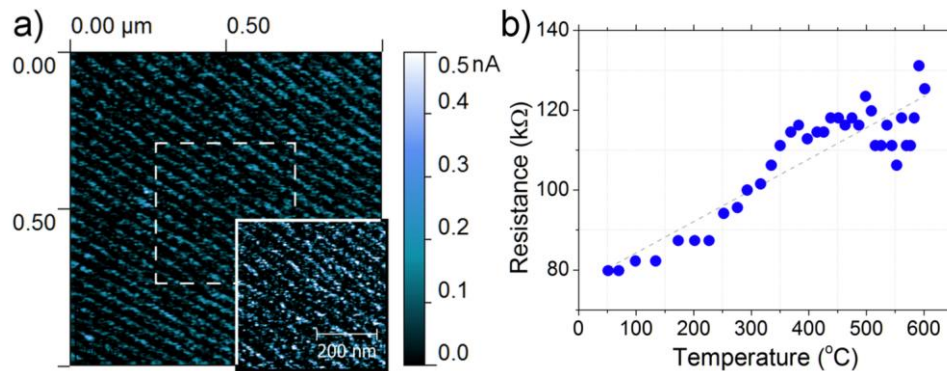

Figure 5. LC-AFM measurements on the STO sample doped with 0.13 at% Fe: (**a**) electrical measurements (current map) in nano-scale, (**b**) resistance vs. temperature in macro-scale after reduction at 1100 °C.

At the same time, the resistance calculated from the LC-AFM measurements is equal to 10^8 Ω for the conducting pattern (brightly colored regions in Figure 5a and 10^{12} Ω for dark regions (low current on the LC-AFM current map). To our knowledge this behavior is unique and was not reported previously for an undoped STO crystal, which suggests that this effect can be connected to the iron doping. Furthermore, standard 2-point method electrical measurement (UHV condition) presents metallic behavior below 700 °C (sample cooled from 1100 °C). The observed changes were significant, however, we decided to go step further and extend the annealing time in order to find any drastic changes in the Fe-doped STO crystal structure and its composition. Thus, the samples were reduced at 1100 °C for up to two days and two additional techniques were used: XRD in standard geometry for phase analysis, and TOF-SIMS which can evaluate micrometer scale composition changes. The results showed that no substantial changes were found as observed by TOF-SIMS depth profiles or XRD phase analysis after 4 h of reduction. However, after 8 h of reduction TOF-SIMS detected 3 μm Ti-rich regions as shown by TOF-SIMS investigation, see Figure 6. Further reduction (24 h) produced even changes in the phase composition that could be detected by the XRD and are shown in Figure 7. Additional phases that could be identified are related to titanium oxides: Ti_2O, Ti_2O_3 and Ti_3O_5 [36]. Interestingly these changes were spotted using standard $\theta - 2\theta$ geometry, which means they are not surface-related but are more bulk-related, thus revealing that prolonged reduction changed the crystal structure significantly.
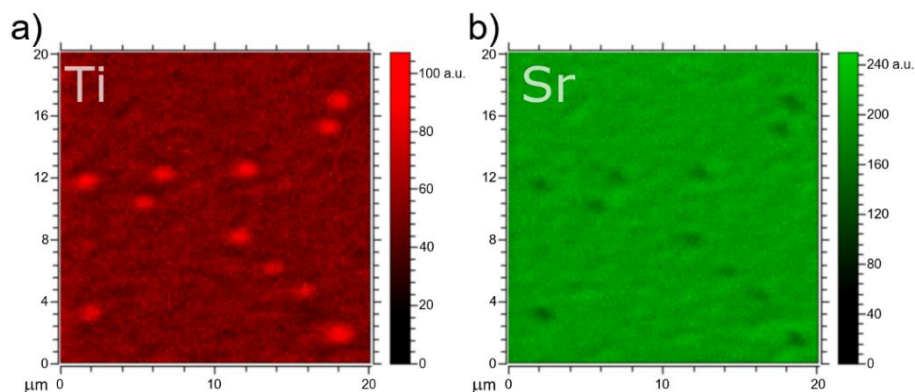
Figure 6. 2D TOF-SIMS chemical composition maps of the Fe-doped STO crystal after reduction at 1100 °C. The different colors correspond to: (**a**) titanium and (**b**) strontium ions. There is an anti-correlation in between Ti and Sr on the surface.
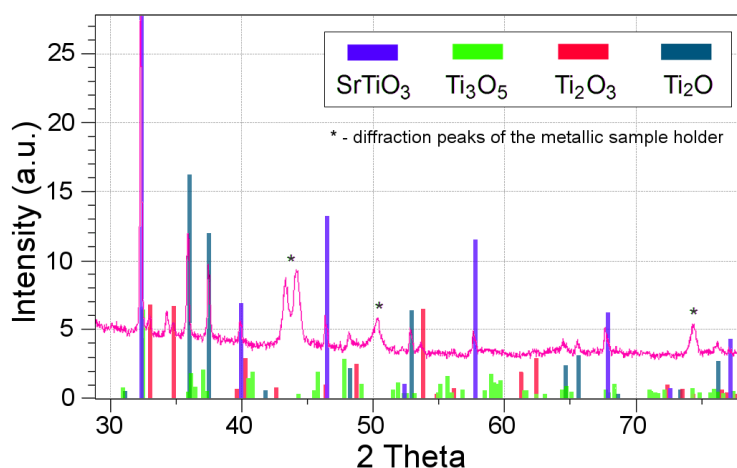

Figure 7. XRD results after 24 h or reduction at 1100 °C of 0.45 % Fe-doped STO sample. The additional phases beside the STO phase are clearly visible.

The XPS investigation provided additional data showing the clear presence of 3+ and 2+ titanium oxidation states—Figure 8a). Furthermore, the Sr *3d* line analysis showed formation of SrO at least on the crystal surface as shown in Figure 8b, however from the XRD data we can evaluate that the changes are reaching the bulk of the crystal. What is more, the crystal samples undergo non-reversible changes during heating cycle. Figure 9 shows two concentration ratios: Sr/Ti and Fe/Ti as measured by the XPS technique. First the samples were reduced at the temperatures up to 1000 °C. During this process, at certain temperatures (250, 500, 750 and 1000 °C) measurements were made. Figure 9a shows Sr/Ti ratio evolution during annealing. The results show relatively stable ratios up to 500 °C. Above that temperature the Sr/Ti ratio changes, showing a drop in the Sr concentration on the crystal surface. The data for the Fe/Ti concentration, shown in Figure 9b, suggest similar behavior for the Fe surface content. Up to 750 °C, the Fe concentration is relatively high, while it decreases drastically between 500 and 750 °C and drops to zero at 1000 °C. During the cooling process, both the Sr and Fe concentration do not return to their original values. The Sr concentration rises to values even higher than for as-received sample, while the Fe concentration remains at close to zero. Thus the iron ions had to migrate into the bulk during the heating procedure. If this was the case, one could find traces of iron ions along a path or a channel leading into the direction of the bulk. To test our prediction we conducted a depth-profiling experiment with the use of TOF-SIMS on 0.13 at% Fe-doped STO sample after short reduction at 1100 °C. Obtained data shows that the Fe concentration (calculated as a FeO/TiO ratio) has a minimum close to the surface and increases into the bulk, which is consistent with the XPS data showing depletion of iron on the surface—Figure 10a. By analyzing the presented

curve, one can see that the iron content is modified at the distance of several hundreds of nm (or more). Furthermore, the data gathered during the depth profiling allowed generation of a 2D map of the Fe distribution towards the bulk shown in Figure 10b.
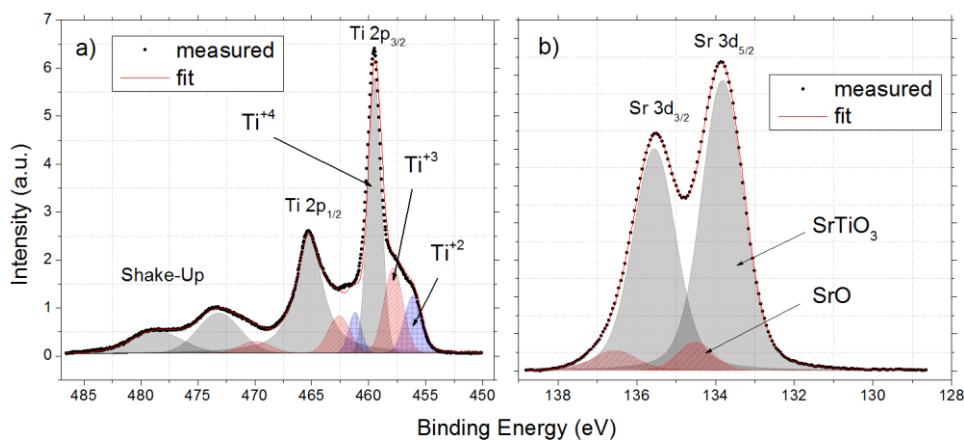

Figure 8. XPS core lines measured at slightly elevated temperature of 200–250 °C on 0.13 at% iron-doped STO sample: (**a**) the Ti *2p* and (**b**) Sr *3d* after extended reduction (24 h).
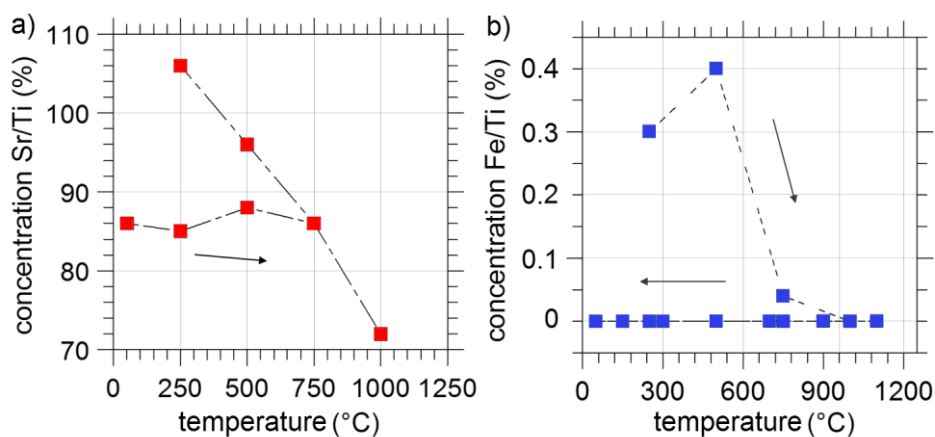

Figure 9. XPS results of the 0.13 at% iron-doped STO sample: (**a**) the Sr/Ti ratio during subsequent heating and cooling cycle, (**b**) the Fe/Ti ratio during one cycle of heating and cooling. The arrows indicate the direction of the temperature cycle.
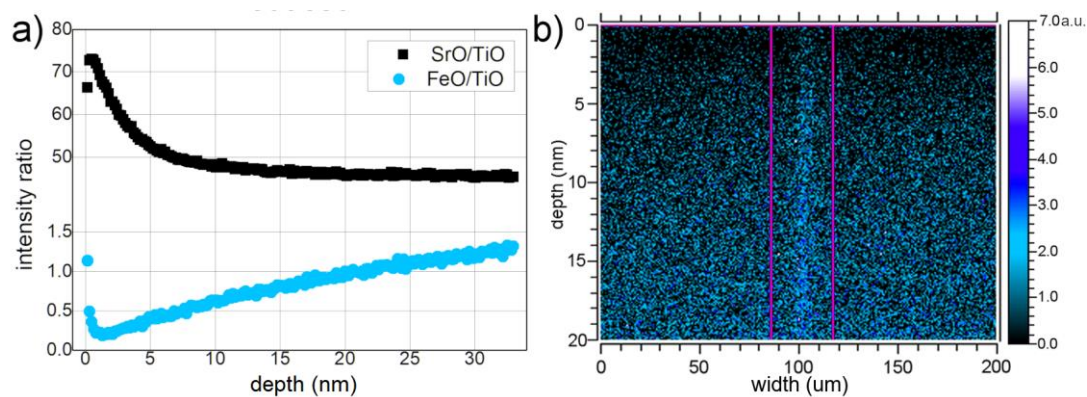

Figure 10. TOF-SIMS depth profiles for 0.13 at% iron-doped STO single crystal after the reduction at 1100 °C: (**a**) the SrO/TiO (black points) and FeO/TiO (blue points) ions ratio towards the bulk and (**b**) the 2D slice from the 3D measurement showing Fe ions concentration in plane perpendicular to the surface.

Indeed, we have measured non-uniform distribution of iron and noticed a number of iron-rich filaments leading from the surface into the bulk. Those filaments were found to be oriented along the [001] direction of the crystal. This is consistent with the fast diffusion paths formed of extended defects found in undoped STO crystals [9,37]. Following the chemical changes, we have decided to investigate the effect of the extended reduction on the topography and local electrical properties of the crystal surface. Using the LC-AFM technique we have found most prominent changes in the 0.45 at% Fe-doped STO samples. Naturally, the extended reduction had significant influence on the surface morphology; we have found that the flat and ordered surface with well visible terraces has disappeared, replaced by the elongated shapes as seen in topography image in Figure 11a. The image shows also the current map measured under relatively low voltage (0.5 V) with features quite similar to 0.13 at% Fe-doped STO sample shown in Figure 5a. Nevertheless, due to long annealing times and composition changes, the observed features are not completely linear, as some distribution of angles is present. In addition, there is a correlation of the local current with the topography, where the well-conducting regions are only found on top of topographical islands. In fact, closer examination of the conducting regions showed that each 'line' is formed of a number of conducting spots ranging from several to tens of nanometers in diameter. Further examination showed that the material between the lines (dark colored regions) is insulating, while the white lines are semiconducting. We have performed current–voltage sweeps (I–V) on those regions, and a typical result is presented in Figure 11b. The I–V curves correspond to different regions, however the y-axis showing flowing current is set to the same values. One can notice that colored lines exhibit semiconductor behavior with the addition of the RS phenomena. The dark regions do not conduct current (current below the detection limit of 700 fA) even with relatively high voltage. They do not exhibit RS behavior either.
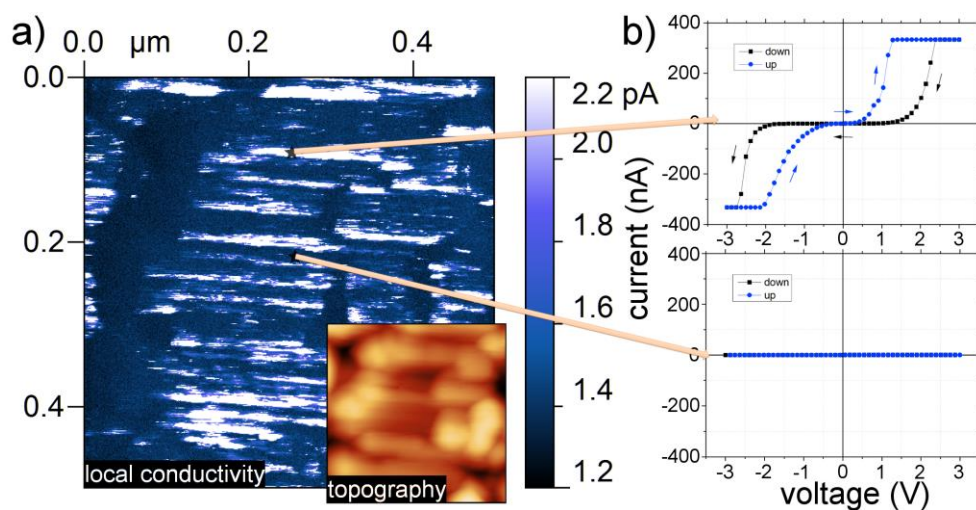

Figure 11. Current map obtained from the LC-AFM measurements for the reduced sample of STO doped with 0.45 at% Fe: (**a**) the local conductivity measured with 500 mV bias along with the topography (inset), and (**b**) the I-V curves showing clear resistive switching behavior (top).

To conclude this section, we have found that the thermal reduction on the Fe-doped STO crystals leads to strong Fe segregation at the temperatures above 700 °C, which results in strong chemical modification of the surface and near-surface region. As one could expect, the modification is more profound the higher the annealing temperature and the longer the reduction time. Additionally, the results of strong topographical and electrical modification were found.

3.3. Annealing under Oxidizing Conditions

The annealing under oxidizing conditions was achieved at a temperature of 1100 °C and 200 mbar O_2 pressure. The results show a strong change in the surface morphology and local current measured

by the LC-AFM. The analysis showed formation of a new phase as shown in the typical topography shown on an example of 0.45 at% Fe-doped crystal shown in Figure 12a. At the same time, the local current maps did not provide any information as the investigated surface become insulating. Even the highest available voltage produced currents lower than 700 fA, which was the lower limit of the current detection in our LC-AFM setup. This information is consistent with the behavior of STO crystals since oxidation removes oxygen vacancies which are responsible for the current conduction in STO. Previously mentioned new phase is formed of relatively large crystallites shown in Figure 12c. Such crystals were already investigated in the STO crystals and are believed to be composed of the SrO phase [38]. Besides the large visible crystals', remaining surface is composed of relatively flat crystal-like surface, with roughens (RMS) close to 4 nm as shown in Figure 12b. This is also consistent with the depth profiles performed by the TOF-SIMS, where increase of the Sr concentration close to the crystal surface is evident as shown in Figure 13a. There is also a sharp increase in the Fe content in the surface region with respect to Ti. In addition, the surface composition was investigated in a form of 2D maps. The results are shown in Figure 13b, where one can notice strong element segregation or even decomposition of the surface in-plane. The Sr and Ti are separated into different regions. The Fe dopant is strongly correlated with Ti regions, as typically it substitutes the Ti in the STO matrix. This correlation is easily visible in multicolored map (overlay of Sr, Ti and Fe) in the right-bottom corner in Figure 13b as purple regions (red–Ti and blue–Fe). Overall, the decomposition of the STO structure into Sr and Ti in a small scale was already observed in other perovskite systems, such as $Ba_xSr_{1-x}TiO_3$ [39,40]. In the last step, a series of XPS spectra after a long reduction and 15 minutes oxidation in air were obtained. This led to the recovery of the 4+ Ti states, and no signs of 3+ or 2+ state were found. Nevertheless, after such cycle no Fe was detected on the surface, thus after migration of the Fe into the bulk, the oxidation process did not reverse this effect as shown in Figure 9b.
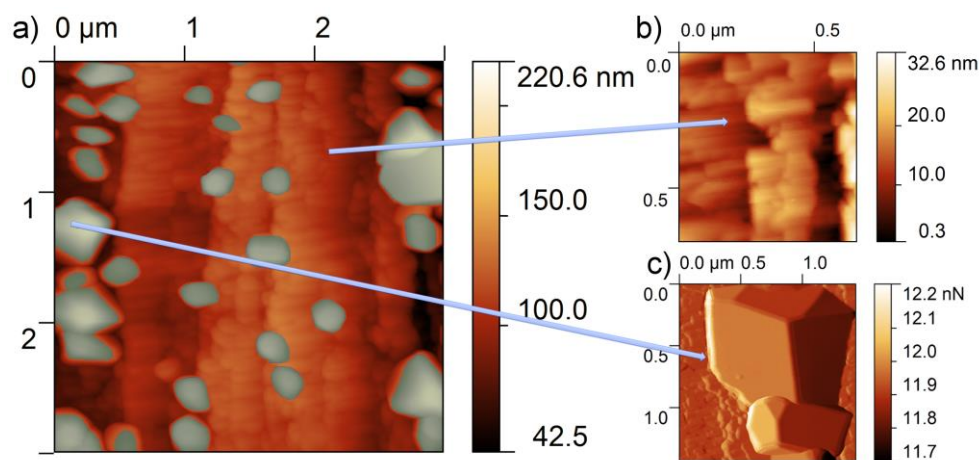

Figure 12. Surface topography obtained by the AFM measurements for the 0.45 at% Fe-doped STO crystal after oxidation: (**a**) typical surface topography, (**b**) magnification of the relatively flat region (**c**) the (normal force) image showing magnification of one of the regions showing clearly visible nanometer-sized crystals.
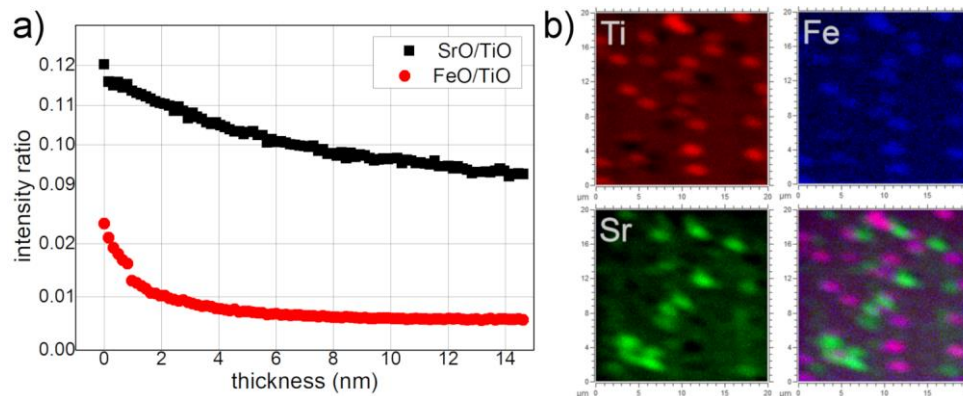
Figure 13. The results of TOF-SIMS investigation on the 0.45 at% Fe-doped STO crystal after oxidation: (**a**) depth profiles showing Sr/Ti and Fe/Ti TOF-SIMS signal ratios, (**b**) 2D chemical composition maps of the Fe-doped STO crystal after oxidation at 1100 °C; different colors correspond to titanium (red), iron (blue), strontium (green) and overlay of Ti, Fe and Sr signals (mixed colors).

To conclude this section, we have found that the oxidation at high temperature on the Fe-doped STO crystals leads to strong Sr and Ti segregation both in-plane and out-of-plane. On one hand, there is depletion of Ti and enrichment of Sr on the surface along with SrO crystals formation, on the other hand, segregation of the Ti and Sr into separate regions. At the same time there is affinity of the Fe to segregate into Ti-rich regions.

4. Conclusions

The measurements performed on single crystals of STO doped with iron (with concentrations up to 0.45 at% Fe) showed inhomogeneous Fe distribution across all concentrations both in as-received and in reduced/oxidized samples. The XRF studies have shown Fe-rich regions, which is most probably related to low solubility of the Fe in STO and high growth rates typical for the Verneuil method. The local conductivity measured by the LC-AFM was also inhomogeneous and an interesting pattern of well-conducting lines was found in reduced crystals. Since the conduction in STO is typically connected to extended defects [4], we assume that the Fe doping is influencing the extended defects' filament formation. Such patterns can be interesting from the application point of view. Furthermore, we investigated the RS behavior and found out that only well-conducting regions exhibited switching. This could suggest that only the regions modified by the inhomogeneous distribution of Fe ions were rich in oxygen vacancy and thus allowed the RS phenomena to occur. The XPS data is in good agreement with our suggestions, showing that the iron ions are in the 2^+ and 3^+ oxidation state only (similar to our previous investigation performed on heavily doped STO epitaxial films [19]). Thus, the oxidation state lower than theoretical 4^+ suggests (or even 3^+) that Fe ions are close to oxygen vacancies. Moreover, all investigated crystals were prone to strong chemical surface instabilities following heat treatment under reducing and oxidizing conditions. Reduction under vacuum at 1100 °C led to formation of new Ti oxide phases and migration of the Fe into the bulk. We have found that starting from 700 °C the Fe ions were highly mobile. Their high mobility can be attributed to the affinity of the Fe ions to the oxygen vacancies. In turn, those vacancies are known to agglomerate along the extended defects, which can act as an easy diffusion path in the STO system. We were able provide proof of that concept by showing a Fe-rich filament structure reaching from the surface into the bulk. On the other hand, the oxidation at 1100 °C led to formation of Sr-rich phases (such as SrO) and strong separation of Ti(Fe) and Sr in the surface region.

References

1. Russo, P.; Xiao, M.; Zhou, N.Y. Electrochemical Oxidation Induced Multi-Level Memory in Carbon-Based Resistive Switching Devices. *Sci. Rep.* **2019**, *9*, 1–10. [CrossRef] [PubMed]

2. Minnekhanov, A.A.; Emelyanov, A.V.; Lapkin, D.A.; Nikiruy, K.E.; Shvetsov, B.S.; Nesmelov, A.A.; Erokhin, V.V.; Vyacheslav, A.D.; Rylkov, V.V. Parylene Based Memristive Devices with Multilevel Resistive Switching for Neuromorphic Applications. *Sci. Rep.* **2019**, *9*, 1–9. [CrossRef] [PubMed]

3. Ielmini, D. Resistive switching memories based on metal oxides: Mechanisms, reliability and scaling. *Semicond. Sci. Technol.* **2016**, *31*, 063002. [CrossRef]

4. Ielmini, D.; Wong, H.S.P. In-memory computing with resistive switching devices. *Nat. Electron.* **2018**, *1*, 333–343. [CrossRef]

5. Zidan, M.A.; Strachan, J.P.; Lu, W.D. The future of electronics based on memristive systems. *Nat. Electron.* **2018**, *1*, 22–29. [CrossRef]

6. Mikhaylov, A.N.; Morozov, O.A.; Ovchinnikov, P.E.; Antonov, I.N.; Belov, A.I.; Korolev, D.S.; Kazantsev, V.B. One-Board Design and Simulation of Double-Layer Perceptron Based on Metal-Oxide Memristive Nanostructures. *IEEE Trans. Emerg. Top. Comput. Intell.* **2018**, *2*, 371–379. [CrossRef]

7. Michalas, L.; Stathopoulos, S.; Khiat, A.; Prodromakis, T. An electrical characterisation methodology for identifying the switching mechanism in TiO_2 memristive stacks. *Sci. Rep.* **2019**, *9*, 1–8. [CrossRef]

8. Kwon, D.H.; Lee, S.; Kang, C.S.; Choi, Y.S.; Kang, S.J.; Cho, H.L.; Kim, M. Unraveling the Origin and Mechanism of Nanofilament Formation in Polycrystalline SrTiO3 Resistive-Switching Memories. *Adv. Mater.* **2019**, *1901322*, 1–12.

9. Szot, K.; Speier, W.; Bihlmayer, G.; Waser, R. Switching the electrical resistance of individual dislocations in single-crystalline $SrTiO_3$. *Nat. Mater.* **2006**, *5*, 312–320. [CrossRef]

10. Szot, K.; Rogala, M.; Speier, W.; Klusek, Z.; Besmehn, A.; Waser, R. TiO_2—A prototypical memristive material. *Nanotechnology* **2011**, *22*, 254001. [CrossRef] [PubMed]

11. Waser, R.; Dittmann, R.; Staikov, G.; Szot, K. Redox-Based Resistive Switching Memories—Nanoionic Mechanisms, Prospects, and Challenges. *Adv. Mater.* **2009**, *21*, 2632–2663. [CrossRef]

12. Szot, K.; Bihlmayer, G.; Speier, W. Chapter Four—Nature of the Resistive Switching Phenomena in TiO_2 and $SrTiO_3$: Origin of the Reversible Insulator–Metal Transition. *Solid State Phys.* **2004**, *65*, 353–559.

13. Sawa, A. Resistive switching in rapid advances in information technology rely on high-speed and large-capacity nonvolatile memories. *Mater. Today* **2008**, *11*, 28–36. [CrossRef]

14. Rodenbücher, C.; Speier, W.; Bihlmayer, G.; Breuer, U.; Waser, R.; Szot, K. Cluster-like resistive switching of $SrTiO_3$: Nb surface layers. *New J. Phys.* **2013**, *15*, 103017. [CrossRef]

15. Hirose, S.; Nakayama, A.; Niimi, H.; Kageyama, K.; Takagi, H. Resistance switching and retention behaviors in polycrystalline La-doped $SrTiO_3$ ceramics chip devices. *J. Appl. Phys.* **2008**, *104*, 053712. [CrossRef]

16. Janousch, M.; Meijer, G.I.; Staub, U.; Delley, B.; Karg, S.F.; Andreasson, B.P. Role of Oxygen Vacancies in Cr-Doped $SrTiO_3$ for Resistance-Change Memory. *Adv. Mater.* **2007**, *19*, 2232–2235. [CrossRef]

17. Wang, J.J.; Huang, H.B.; Bayer, T.J.M.; Moballegh, A.; Cao, Y.; Klein, A.; Chen, L.Q. Defect chemistry and resistance degradation in Fe-doped $SrTiO_3$ single crystal. *Acta. Mater.* **2016**, *108*, 229–240. [CrossRef]

18. Szot, K.; Speier, W. Surfaces of reduced and oxidized $SrTiO_3$ from atomic force microscopy. *Phys. Rev. B* **1999**, *60*, 5909–5926. [CrossRef]

19. Szot, K.; Speier, W.; Carius, R.; Zastrow, U.; Beyer, W. Localized Metallic Conductivity and Self-Healing during Thermal Reduction of $SrTiO_3$. *Phys. Rev. Lett.* **2002**, *88*, 2–5. [CrossRef]

20. Blanc, J.; Staebler, D.L. Electrocoloration in $SrTiO_3$: Vacancy Drift and Oxidation-Reduction of Transition Metals. *Phys. Rev. B* **1971**, *4*, 3548–3557. [CrossRef]

21. Menke, T.; Meuffels, P.; Dittmann, R.; Szot, K.; Waser, R. Separation of bulk and interface contributions to electroforming and resistive switching behavior of epitaxial Fe-doped SrTiO$_3$. *J. Appl. Phys.* **2009**, *105*, 066104. [CrossRef]

22. Chen, X.G.; Ma, X.B.; Yang, Y.B.; Chen, L.P.; Xiong, G.C.; Lian, G.J.; Yang, J.B. Comprehensive study of the resistance switching in SrTiO$_3$ and Nb-doped SrTiO$_3$. *Appl. Phys. Lett.* **2011**, *98*, 122102. [CrossRef]

23. Leonarska, A.; Szot, K.; Ratuszna, A. Temperature evolution of the crystal structure in SrTiO$_3$ doped by W^{6+}, Ni^{3+}, Fe^{3+} and La^{3+}. *Phase Transit.* **2011**, *84*, 1015–1027. [CrossRef]

24. Faughnan, B. Photochromism in Transition-Metal-Doped SrTiO$_3$. *Phys. Rev. B* **1971**, *4*, 3623–3636. [CrossRef]

25. Lenser, C.; Kalinko, A.; Kuzmin, A.; Berzins, D.; Purans, J.; Szot, K.; Dittmann, R. Spectroscopic study of the electric field induced valence change of Fe-defect centers in SrTiO$_3$. *Phys. Chem. Chem. Phys.* **2011**, *13*, 20779–20786. [CrossRef]

26. Wojtyniak, M.; Szot, K.; Wrzalik, R.; Rodenbücher, C.; Roth, G.; Waser, R. Electro-degradation and resistive switching of Fe-doped SrTiO$_3$ single crystal. *J. Appl. Phys.* **2013**, *113*, 083713. [CrossRef]

27. Berney, R.; Cowan, D.; Morin, F. ESR of Fe^{3+}-Rhombic, Fe^{2+}-Vo and Fe^{1+}-Vo complexes in SrTiO$_3$. *Solid State Commun.* **1978**, *26*, 579–582. [CrossRef]

28. Kool, T.; Glasbeek, M. Electron paramagnetic resonance of photochromic Fe^{2+}-O-in SrTiO$_3$. *J. Phys. Condens. Matter* **1993**, *5*, 361–370. [CrossRef]

29. Szade, J.; Szot, K.; Kulpa, M.; Kubacki, J.; Lenser, C.; Dittmann, R.; Waser, R. Electronic structure of epitaxial Fe-doped SrTiO$_3$ thin films. *Phase Transit.* **2011**, *84*, 489–500. [CrossRef]

30. Kohl, A.; Kajewski, D.; Kubacki, J.; Lenser, C.; Dittmann, R.; Meuffels, P.; Szade, J. Detection of Fe^{2+} valence states in Fe doped SrTiO$_3$ epitaxial thin films grown by pulsed laser deposition. *Phys. Chem. Chem. Phys.* **2013**, *15*, 8311–8317. [CrossRef]

31. Drahus, M.D.; Jakes, P.; Erdem, E.; Eichel, R.-A. Defect structure of the mixed ionic–electronic conducting Sr[Ti,Fe]O$_x$ solid-solution system—Change in iron oxidation states and defect complexation. *Solid State Ion.* **2011**, *184*, 47–51. [CrossRef]

32. Adler, P.; Lebon, A.; Damljanović, V.; Ulrich, C.; Bernhard, C.; Boris, A.V.; Keimer, B. Magnetoresistance Effects in SrFeO$_3-\delta$: Dependence on Phase Composition and Relation to Magnetic and Charge Order. *Phys. Rev. B* **2006**, *73*, 1–50. [CrossRef]

33. Bocquet, A.; Fujimori, A.; Mizokawa, T.; Saitoh, T.; Namatame, H.; Suga, S.; Takano, M. Electronic Structure of SrFe^{4+}O$_3$ and Related Fe Perovskite Oxides. *Phys. Rev. B* **1992**, *45*, 1561. [CrossRef] [PubMed]

34. Kawasaki, M.; Takahashi, K.; Maeda, T.; Tsuchiya, R.; Shinohara, M.; Ishiyama, O.; Yonezawa, T.; Yoshimoto, M.; Koinuma, H. Atomic Control of the SrTiO$_3$ Crystal Surface. *Science* **1994**, *266*, 1540–1542. [CrossRef] [PubMed]

35. Rodenbücher, C.; Wojtyniak, M.; Szot, K. *Conductive AFM for Nanoscale Analysis of High-k Dielectric Metal Oxides*; Springer: Cham, Switzerland, 2019.

36. Strachan, J.P.; Pickett, M.D.; Yang, J.J.; Aloni, S.; David Kilcoyne, A.L.; Medeiros-Ribeiro, G.; Stanley Williams, R. Direct Identification of the Conducting Channels in a Functioning Memristive Device. *Adv. Mater.* **2010**, *22*, 3573–3577. [CrossRef] [PubMed]

37. Rodenbücher, C.; Menzel, S.; Wrana, D.; Gensch, T.; Korte, C.; Krok, F.; Szot, K. Current channeling along extended defects during electroreduction of SrTiO$_3$. *Sci. Rep.* **2019**, *9*, 1–9.

38. Szot, K.; Speier, W.; Herion, J.; Freiburg, C. Restructuring of the surface region in SrTiO$_3$. *Appl. Phys. A Mater. Sci. Process.* **1996**, *64*, 55–59. [CrossRef]

39. Tenne, D.; Soukiassian a Zhu, M.; Clark a Xi, X.; Choosuwan, H.; Bhalla, A. Raman study of Ba$_x$Sr$_{1-x}$TiO$_3$ films: Evidence for the existence of polar nanoregions. *Phys. Rev. B* **2003**, *67*, 012302. [CrossRef]

40. Fuks, D.; Dorfman, S.; Piskunov, S.; Kotomin, E. Ab initio thermodynamics of Ba$_c$Sr$_{(1-c)}$TiO$_3$ solid solutions. *Phys. Rev. B* **2005**, *71*, 014111. [CrossRef]